Regional Studies in Marine Science 24 (2018) 336–342

Contents lists available at ScienceDirect

Regional Studies in Marine Science

journal homepage: www.elsevier.com/locate/rsma

The dynamics of weather-band sea level variations in the Red Sea

James H. Churchill [a,*], Yasser Abualnaja [b], Richard Limeburner [a], Mohammedali Nellayaputhenpeedika [c]

[a] Department of Physical Oceanography, Woods Hole Oceanographic Institution, Woods Hole, MA 02543, USA
[b] Red Sea Research Center, King Abdullah University of Science and Technology, Thuwal, Saudi Arabia
[c] Department of Marine Science, Bharathidasan University, Tiruchirappalli 620024, India

HIGHLIGHTS

- A sizable fraction of sea level motion in the Red Sea occurs in the 'weather-band' (~4-30 d period).
- A single mode of motion dominates the weather-band sea level signal over the Red Sea.
- In this mode, the water level rises and falls coherently over the full Red Sea.
- Short-term sea level motions of this dominant mode are predicted by 1-D barotropic model.

ARTICLE INFO

Article history:
Received 20 December 2017
Received in revised form 7 September 2018
Accepted 17 September 2018
Available online 27 September 2018

Keywords:
Red Sea water levels
Wind-driven sea level variations

ABSTRACT

The variations of sea level over the Red Sea may be divided into three broad categories: tidal, seasonal and weather-band. Our study employs a variety of in situ and satellite-derived data in the first comprehensive examination of the Red Sea water level variations in the weather-band (covering periods of ~4–30 days). In the central Red Sea, the range of the weather-band sea level signal is of order 0.7 m, which exceeds the tidal and seasonal sea level ranges. From EOF and correlation analysis, we find that a large fraction of the weather-band sea level variation is due to a single mode of motion that extends over the entire Red Sea. In this mode, the water level rises and falls in unison with an amplitude that declines going southward over the southern Red Sea. The temporal signal of this mode is highly correlated with the along-axis surface wind stress over the southern Red Sea, and is closely reproduced by a simple one-dimensional barotropic model with forcing by the along-axis wind stress. Although this model does not account for the full suite of dynamics affecting weather-band sea level variations in the Red Sea, it may serve as a useful predictive tool. Sea level changes associated with the development and movement of sub-mesoscale features (e.g., eddies and boundary currents) are also shown to contribute to weather-band sea level motions in the Red Sea.

1. Introduction

As reported by Sultan et al. (1995), variations in water level of the central Red Sea span a range of order 1 m. Though relatively modest compared with surface excursions in many coastal areas, sea level changes of this magnitude may critically impact shallow ecosystems of the Red Sea. Perhaps foremost among the environments that may be affected by order 1-m water level changes are the crests of platform reefs, which are prevalent in the Red Sea and are typically at mean depths of 1–2 m (DeVantier et al., 2000; Bruckner et al., 2012). Order 1-m water level variations will affect the thermal environment over such reefs by altering the ratio of the water volume to the surface area (subject to surface heat exchange) over the reef crest (e.g., Davis et al., 2011). As revealed by a number of investigators, hydrodynamics over shallow reef crests are sensitive to water level changes (e.g., McDonald et al., 2006; Monismith et al., 2013; Lentz et al., 2016, 2017). In particular, the analysis of Lentz et al. (2017) indicates that the drag coefficient for depth-averaged flow over a platform reef strongly depends on mean depth, with the drag coefficient varying by an order of magnitude over a depth range of 0.2–2 m. The alteration of the thermal and hydrodynamic regimes due to sea level changes over a platform reef will, in turn, impact the reef ecosystem by influencing temperature variations and rate of flow over the reef.

Considerable scientific attention has been directed at Red Sea water level changes at tidal and seasonal frequencies. It is well established that tides in the Red Sea are predominately semidiurnal, with $[(K_1 + O_1)/(M_2 + S_2)] < 0.25$ (Vercelli, 1925; Defant, 1961; Morcos, 1970; Madah et al., 2015; Pugh and Abualnaja, 2015), and that the M_2 tidal constituent has an amphidromic point in the

* Corresponding author.
E-mail address: jchurchill@whoi.edu (J.H. Churchill).

https://doi.org/10.1016/j.rsma.2018.09.006

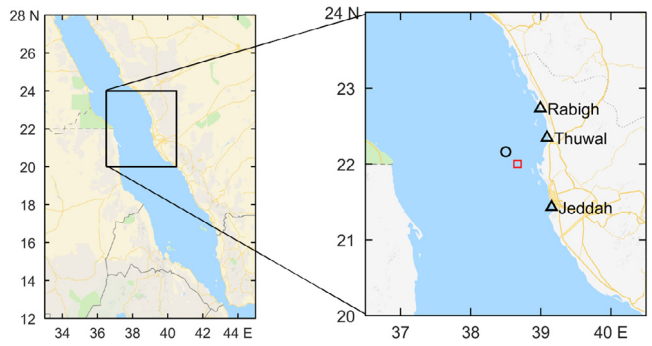

Fig. 1. Map of the full Red Sea (left) and central Red Sea (right) showing sites of this study's pressure sensors (triangles), the central Red Sea meteorological buoy (circle) and the GEOS/DAS wind record closest to the meteorological buoy (red square).

central Red Sea near 20°N. Consequently, the tidal amplitude varies considerably over the length of the Red Sea, increasing from less than 0.25 m over the central Red Sea to more than 0.5 m at the northern and southern extremes (Morcos, 1970; Jarosz et al., 2005; Madah et al., 2015; Pugh and Abualnaja, 2015).

The seasonal variation of Red Sea water level is marked by higher surface elevations in winter than in summer. The range of the seasonal water level signal is roughly constant at 0.3–0.4 m over the central and northern Red Sea (Morcos, 1970; Sultan et al., 1995, 1996; Abdelrahman, 1997; Sofianos and Johns, 2001; Manasrah et al., 2009), but declines over the southern Red Sea to a magnitude of roughly 0.2 m near Bab al Mandab (Sofianos and Johns, 2001). According to the analysis of Sofianos and Johns (2001), based on a simple 1-dimensional momentum balance (ignoring the Coriolis effect and bottom friction), the along-axis wind stress is the principal driver of the seasonal sea level signal over all but the extreme southern portion of the Red Sea (south of 14°N) where the steric contribution dominates.

To date, the variation of Red Sea water levels in the frequency band between the tidal and seasonal frequencies has not been subject to in-depth scientific scrutiny. In the study described here, we find that sea level variations in this intermediate band significantly contribute to the overall water level signal of the central Red Sea. We utilize in situ pressure measurements as well as satellite-derived sea level anomaly (SLA) fields to describe the spatial character of sea level motions in this band, which we refer to as the weather-band as most of the sea level variance in the band occurs over the range of periods (4–30 days) over which weather-related fluctuations dominate atmospheric records. Employing a one-dimensional momentum balance and reanalysis winds, we devise a simple model for the short-term prediction of sea level variations in the weather-band.

2. Data and methods

In situ records of water level used in our study were from Seabird SBE26 Seagauge pressure gauges deployed in the central Red Sea off the coast of Saudi Arabia and set to record pressure at 5-min intervals. From north to south, the deployment locations were offshore of: Rabigh, Thuwal, and Jeddah (Fig. 1). Unfortunately, each record contained a number of gaps. Our analysis largely focused on the period of 1 May 2008–1 May 2011 during which there were no gaps in the pressure time series from the three sites.

Our study also employed in situ wind measurements from an anemometer (Gill Instruments WindObserver II Ultrasonic Anemometer) mounted at 3.5 m above sea level on a meteorological buoy deployed in the central Red Sea basin (Fig. 1) from mid October 2008 through early December 2010 (Farrar et al., 2009; Bower and Farrar, 2015). The anemometer wind record was converted to surface stress using the formulae of Large and Pond (1981).

To examine water level fields over the entire Red Sea, we downloaded SLA data from AVISO (http://www.aviso.oceanobs.com/). Referenced with respect to the CLS01 (Centre de Localisation des Satellites) long-term mean sea surface height, the fields supplied by AVISO were determined by combining sea level data from all available satellites and objectively mapping SLA on a 0.25° latitude by 0.25° longitude grid and at a time interval of one day.

Large-scale wind fields used in our study were produced by version 5.2.0 of the Goddard Earth Observing System (GEOS) atmospheric model and data assimilation system (DAS). The GEOS/DAS wind records were from a 30′ latitude by 40′ longitude grid and were spaced in time at a 6-h interval. Surface wind stress was computed from the GEOS/DAS winds using the formulae of Large and Pond (1981).

To assess the GEOS/DAS wind data, we compared the along-axis (at 153°T) wind stress determined from the meteorological buoy's wind record with the along-axis wind stress computed from the GEOS/DAS wind record closest to the buoy (Fig. 1). The two wind stress records were highly correlated, with R = 0.85 and a linear regression slope of 1.0.

Culling the tidal and seasonal signals from the pressure records (leaving the weather-band signal) was done in three steps. First, the tidal signal was removed using a 4-day half-power point filter (known as the pl66 filter; Limeburner, 1985). Second, the seasonal (1-yr period) signal was estimated by applying a nonlinear least-squares regression technique (with MATLAB function *nlinfit*) to the filtered pressure series. Third, the estimated seasonal signal was subtracted from the filtered time series leaving the intermediate, or weather-band, signal (see Fig. 2).

The weather-band signal was extracted from the SLA records by estimating and then subtracting each record's seasonal signal, determined as described above. It should be noted that the SLA records do not capture the full range of sea level motion in the weather-band. Comparison of the frequency spectra derived from the records of SLA and pressure reveals that the SLA records contain very little of the sea level signal over the higher frequency portion of the weather-band. At periods <11 days, the spectral density of the SLA motions is lower than the spectral density of the motions recorded by the pressure sensors by a factor of >5. At periods of >15 days, the spectral density of the SLA and pressure records are comparable. To ensure that we were comparing motions of similar frequency content when correlating SLA- and pressure-derived weather-band signals, we first filtered the weather-band signal of the pressure records (determined as described above) with a 15-d half-power point filter.

In essence, the limitation of the SLA data required us to consider the sea level motions in two frequency bands. One is the full weather-band, which encompasses the range of periods between the tidal and seasonal signals (roughly 4–30 days). The second is the lower-frequency portion of the weather-band (referred to as LFWB), which encompasses periods of roughly 15–30 days. Fortunately, much of the sea level variance of the weather-band is contained in this lower-frequency portion, which is captured by the SLA records. Filtering the pressure-derived weather-band signal with the 15-d half-power point filter reduced the signal's variance by only 33%.

3. Results

3.1. Characteristics of the weather-band sea level signal in the central Red Sea

The Seagauge data from all three measurement locations show pressures with an overall range of roughly 1.25 db (= 1.25 m).

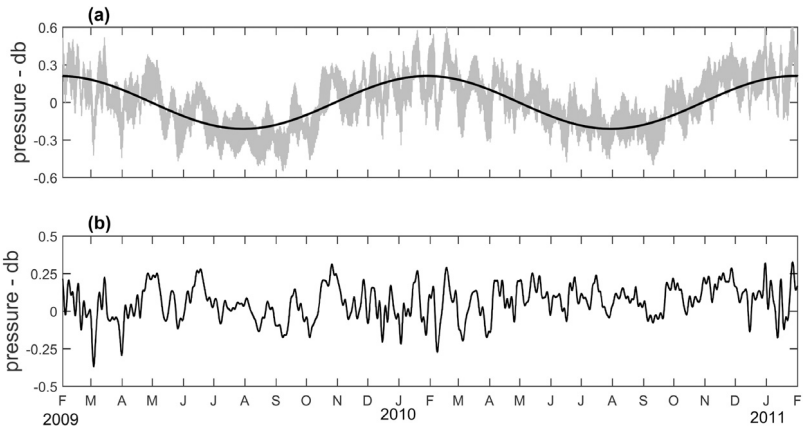

Fig. 2. Example of the pressure signal measured in the central Red Sea and its components. (a) The unfiltered pressure record measured by the Seagauge off Thuwal (Fig. 1) and seasonal pressure signal derived by fitting a 1-yr period sinusoid to the pressure record. (b) The portion of the pressure signal in the frequency band between the tidal and seasonal bands.

Water level motion in the weather-band is the greatest contributor to the pressure variation (Fig. 2). At all locations, the range of the weather-band pressure signal, at ∼0.70 db, exceeds the range of the tidal (∼0.54 db) and seasonal signals (∼0.42 db). Motions in the weather-band span a range of time scales. Prominent (order 0.5 m) sea level excursions occur over time intervals of 20–30 days (i.e., in April–May, June and October 2009 in Fig. 2b) and over intervals of <10 days (i.e., in early March 2009 and early February 2010, Fig. 2b).

The weather-band pressure signals from the three sites are highly correlated with one another (R > 0.98 and slope = 1.0). In view of these high correlations, the results presented below are from the Thuwal (central) pressure record only.

Inspection of the weather-band pressure records reveals a seasonality marked by higher variance in winter relative to spring. To quantify this, we determined the standard deviation of the weather-band pressure signal over a 90-day window, which was stepped through the weather-band pressure record. Over a 6-year period, the standard deviation at the center of the moving window (Fig. 3b) shows a clear seasonal signal, marked by a minimum of ∼0.06 db in summer (July–August) and a maximum of ∼0.13 db in winter (February–March).

The variation of the GEOS/DAS wind stress at sites near the pressure gauges exhibits a similar seasonality, as shown by the standard deviation record of the along-axis wind stress determined in a 90-day moving window (Fig. 3a). This standard deviation record of the wind stress mirrors the standard deviation record of the weather-band pressure, showing minima of ∼0.3 Pa in summer and maxima of ∼0.6 Pa in winter.

3.2. The large-scale weather-band signal

The SLA records are well suited to examine the spatial structure of the sea level fluctuations over the full Red Sea. The correlation scale of LFWB sea level fluctuations is illustrated here by the level of correlation of the LFWB signal of the Thuwal pressure record with the LFWB signal of each SLA record (Fig. 4a). Points at which the LFWB SLA signal is highly correlated (at R > 0.8) with the Thuwal LFWB pressure signal extend over nearly the full length of the Red Sea (from 14 to 28°N) (Fig. 4a). The correlations are not spatially uniform, however. There are distinct areas of reduced correlation (R ∼ 0.7) (e.g., areas centered at ∼22 and 24°N). We deal with possible causes for the reduced correlation in these areas in Section 3.5.

The long correlation length scale of the LFWB sea level signal shown in Fig. 4a, suggests that the sea level motions in the LFWB may be largely due to a coherent mode of motion extending over most of the Red Sea. To quantify the spatial structure of the weather-band sea level fluctuations, we decomposed the LFWB SLA signal over the Red Sea into Empirical Orthogonal Functions (EOFs) through

$$SLA\,(x,\,t) = \sum_{k=1}^{M} S_k\,(x)\,T_k(t) \qquad (1)$$

where *SLA(x,t)* is the LFWB SLA at location x and time t, and S_k and T_k are spatial and temporal functions of mode k determined from SLA records from M locations.

The results show that the LFWB sea level fluctuations over the Red Sea are dominated by a single mode, which accounts 73% of the overall LFWB SLA variance. Notably, the spatial function of this first mode has the same sign at all locations (Fig. 4b), indicating that sea level motion accounted for by this mode rises and falls in phase over the full Red Sea. The modal amplitude is roughly constant over the northern and central Red Sea, and declines sharply (by a factor of 2) going southward over the southern Red Sea. The first-mode time series is correlated with the LFWB Thuwal pressure signal at R = 0.91, implying that 82% of the LFWB sea level variance measured by the Thuwal pressure sensor is due to motions represented by the first-mode EOF.

3.3. Correlation with surface wind stress

It is well established that the large-scale wind directed along the Red Sea's main axis varies in a distinct seasonal cycle (Patzert, 1974; Sofianos and Johns, 2001). From late spring through early autumn, along-axis winds from the NNW tend to prevail over the entire Red Sea. During the rest of the year, along-axis winds tend to be from the SSE over the southern Red Sea and from the NNW over the northern Red Sea, with a zone of wind convergence in the 18–20°N latitude range (Patzert, 1974; Sofianos and Johns, 2001). This pattern is apparent in the GEOS/DAS wind data (Fig. 5). Along-axis GEOS/DAS winds averaged over the 25–26°N latitude band (in the northern Red Sea) are predominately from the NNW (negative in Fig. 5) during all seasons, with a mean of ∼5 m s^{-1}. By contrast, along-axis GEOS/DAS winds averaged over the 16–17°N latitude band exhibit a seasonal variation, switching from NNW in the summer to SSE in the winter. The seasonal signal of the southern Red Sea winds has an amplitude of roughly 4 m s^{-1}. Superimposed on this seasonal signal are large weather-band variations of along-axis winds with magnitudes reaching 15 m s^{-1}. Weather-band variations of smaller magnitude (with roughly $\frac{1}{2}$ the variance) appear in the along-axis wind records of the northern Red Sea. The weather-band variations of along-axis wind over the northern and

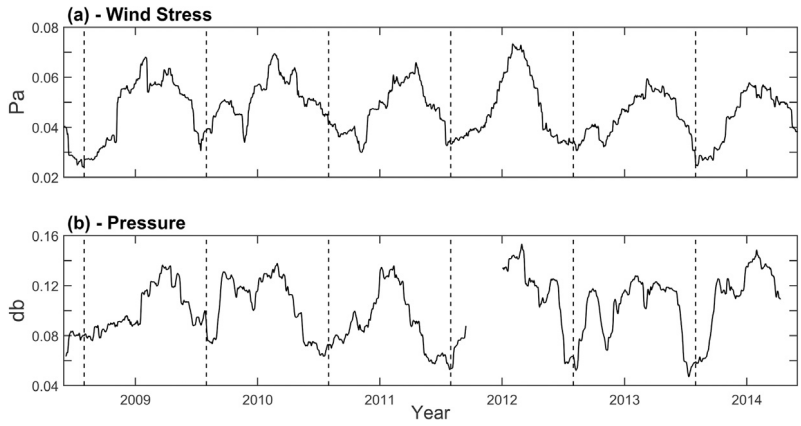

Fig. 3. Plots showing seasonality of wind stress and weather-band sea level fluctuations in the central Red Sea. (a) Running standard deviation (over a 90-day window) of the along-axis wind stress (determined from GEOS/DAS winds at the location of the square in Fig. 1). (b) Running 90-day standard deviation of the weather-band portion of the Thuwal pressure record. The vertical dashed lines are at 1 August of each year.

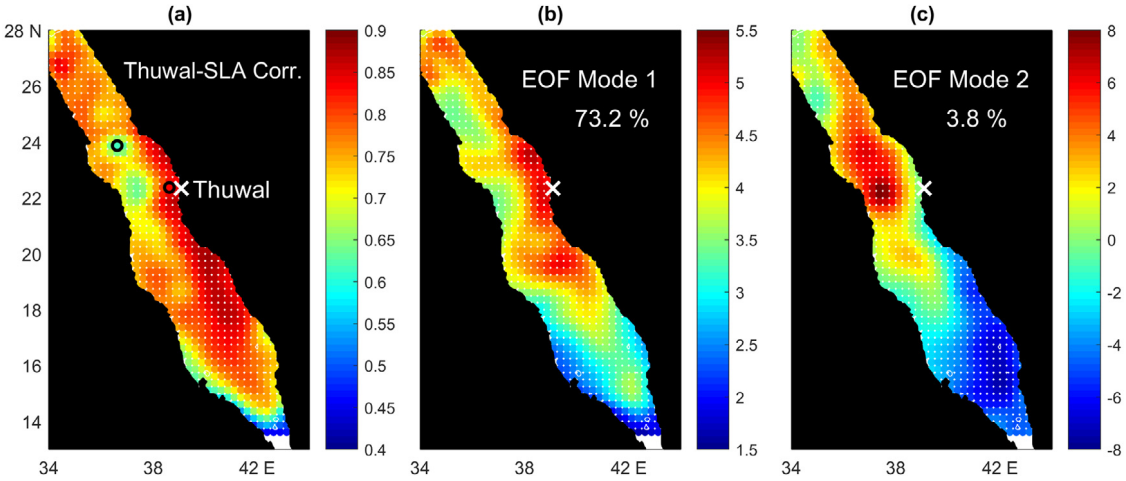

Fig. 4. Horizontal structure of the low-frequency weather-band (LFWB) sea level fluctuations over the Red Sea. Shown in (a) are the correlations of LFWB sea level anomaly (SLA) fluctuations with the LFWB pressure signal measured near Thuwal (at the white x). All correlations are significant at the 95% level. Shown in (b, c) is the spatial structure of the 1st and 2nd mode EOFs computed from the LFWB SLA records. The percent of overall variance accounted for each mode is indicated. The black circles in (a) enclose points at which the SLA series are compared.

southern Red Sea are weakly correlated ($R^2 = 0.17$ for the two series shown in Fig. 5 with the seasonal signals removed).

To quantify the relationship between LFWB sea level variations and the surface wind stress, we carried out linear correlation analysis relating the LFWB portion of the surface wind stress determined from each GEOS/DAS record with the LFWB variations of the Thuwal pressure record and with the time series of the first EOF of the LFWB SLA fluctuations. The correlations were carried out for all wind directions (in 5° increments) and for lags (with wind stress leading) from 0 to 8 days.

For all wind stress records, the maximum wind-EOF or wind-pressure correlation occurs at a wind direction very close to the orientation of the Red Sea axis (153°T). Including all wind records, the mean ratio of the maximum correlation with the along-axis wind to the overall maximum correlation (over all wind directions) is 0.96 for the wind-pressure correlation and 0.95 for the wind-EOF correlation.

The correlations of the along-axis wind stress with both the first-mode EOF and the Thuwal pressure record (Fig. 6) indicate that the weather-band sea level fluctuations may be far more effectively forced by along-axis winds over the southern, rather than the northern, Red Sea. The average correlation between the LFWB along-axis wind stress and the Thuwal pressure record is 0.76 for winds from the 14 to 18°N band and only 0.26 for winds from the 24 to 28°N band. A similar difference seen in the averages of wind-EOF correlations.

3.4. A simple model of wind forcing

Based on the above analysis, it appears that the along-axis wind may be key in driving the weather-band sea level variations over the Red Sea. The analysis of Sofianos and Johns (2001) demonstrated that the wind-driven seasonal sea level signal over the Red Sea could be accounted for by a simple one-dimensional barotropic momentum balance. Prompted by their findings, we sought to determine if the observed weather-band water level fluctuations of the Red Sea conform to a simple barotropic model of forcing by the along-axis wind. The model was formed by combining the along-axis momentum balance and the equation of volume conservation:

$$\frac{\partial U}{\partial t} = -g\frac{\partial \delta}{\partial x} + \frac{\tau_{Sx}}{\rho H} \tag{2}$$

$$\frac{\partial \delta}{\partial t} = H\frac{\partial U}{\partial x} \tag{3}$$

where x is the along-axis coordinate, t is time, ρ is a characteristic water density, g is gravitation acceleration, δ is sea level elevation

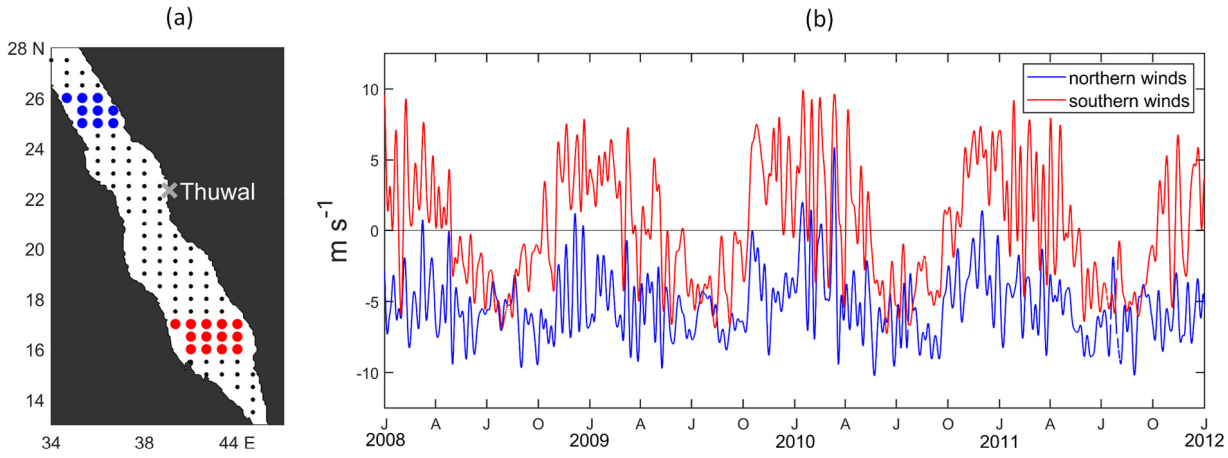

Fig. 5. Plot of along-axis (27° CCW of N) winds averaged over latitude bands of 16–17 and 25–26°N. The winds are averages of GEOS/DAS winds from the stations marked with red and blue dots in (a) (other GEOS/DAS stations are marked with black dots) . (For interpretation of the references to color in this figure legend, the reader is referred to the web version of this article.)

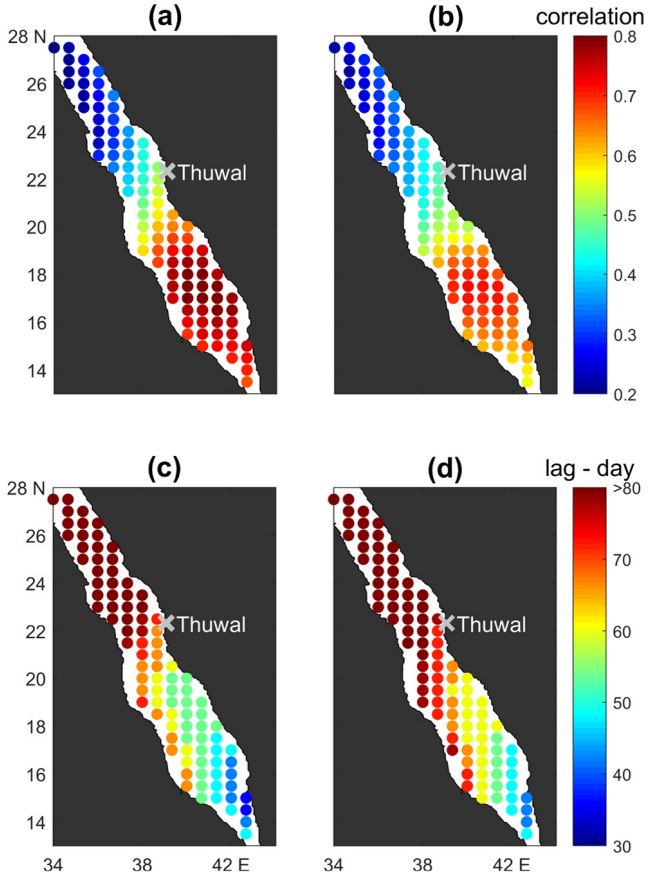

Fig. 6. Results of linear correlation analysis relating LFWB variations in the along-axis surface wind stress with LFWB variations in the Thuwal pressure record (a and c) and with the time series of the first-mode EOF of the LFWB variations of SLA (b and d). Panels a and b show the maximum correlations, which occur at the lags (wind leading) shown in panels c and d.

relative to the long-term mean, U is the vertically averaged along-axis velocity over a depth, H, and τ_{Sx} is the surface wind stress. As with the model of Sofianos and Johns (2001), bottom friction and the effect of the earth's rotation have been ignored.

The above equations were numerically solved for δ over a series of 100-km long bands spanning the length of the Red Sea. The surface wind stress time series applied to each band was taken as the average along-axis wind stress series determined from all GEOS/DAS wind records within the band. Before averaging, the wind stress records were filtered to retain only the weather-band fluctuations. At the southern boundary, δ was held at zero, while U was set to zero at the northern boundary.

The best comparison of the weather-band variations of the Thuwal pressure record with the computed δ within the 100-km band encompassing Thuwal (δ_{Th}) is achieved with $H = 55$ m (Fig. 7). This depth roughly corresponds to the top of the permanent pycnocline of the Red Sea (Morcos, 1970; Sofianos and Johns, 2007), implying that the response to weather-band wind forcing may principally occur above the permanent pycnocline. The model of Sofianos and Johns produced a similar result, with the optimal model-to-observed sea level comparison produced with a model depth of 25 m.

Nevertheless, there are two primary concerns that cast doubt on the applicability of a one-dimensional barotropic model to account for the dynamics of wind-driven sea level motions in the weather-band. One is the phase differences between the observed and modeled sea level fluctuations. The maximum correlation between δ_{Th} and the weather-band Thuwal pressure record equals 0.84 and occurs at a lag of 47 h with δ_{Th} leading. The second concern is with the omission of the Coriolis term, $f\,V$ (where f is the Coriolis frequency and V is the vertically averaged across-axis velocity), in (2). It has been shown (e.g., Csanady, 1973) that this may be neglected in a barotropic model if the width of the system being modeled is considerably smaller than the barotropic radius of deformation:

$$R = \frac{\sqrt{gH}}{f}. \tag{4}$$

For $f = 0.52 \times 10^{-4}$ s^{-1} (value at 21°N) and $H = 55$ m, $R = 450$ km, which is larger, but not considerably so, than the order 250 km width of the Red Sea. We thus conclude that while the simple model of (2) and (3) may be useful in predicting weather-band sea level variations (due to the 2-day lead of the modeled-to-observed sea level), fully understanding the response of the Red Sea water level to weather-band wind forcing will require a more sophisticated model.

3.5. The contribution of mesoscale features

In contrast to the first-mode EOF of weather-band sea level variations, which is uniform in sign over full Red Sea, higher EOF

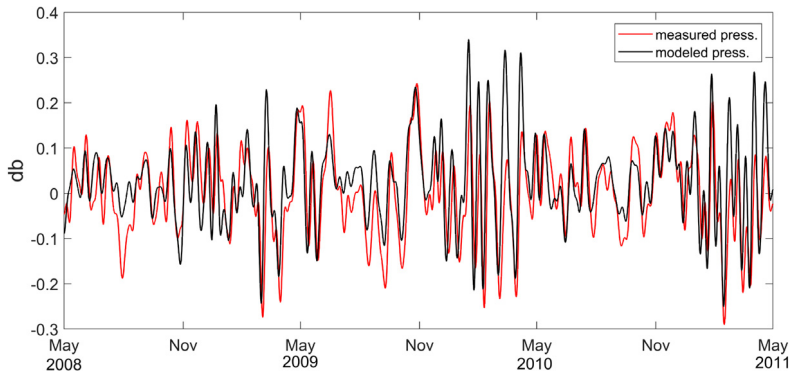

Fig. 7. Comparison of measured and modeled weather-band pressure fluctuations at Thuwal (Fig. 1).

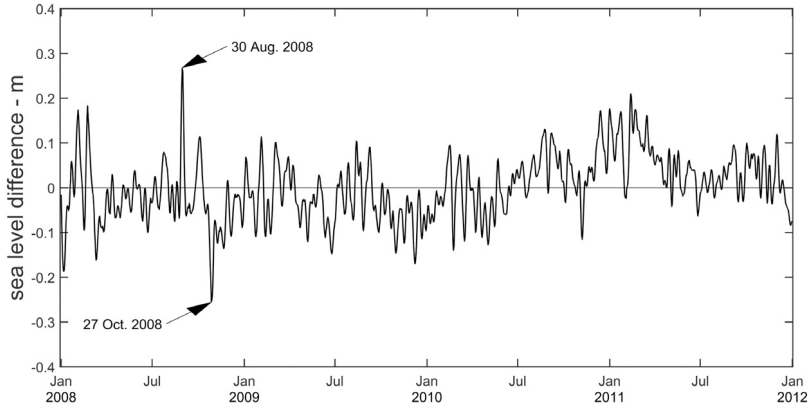

Fig. 8. Difference between the SLA at the two points shown in Fig. 4a. Events of large differences on 30 Aug. and 27 Oct. 2008 are indicated.

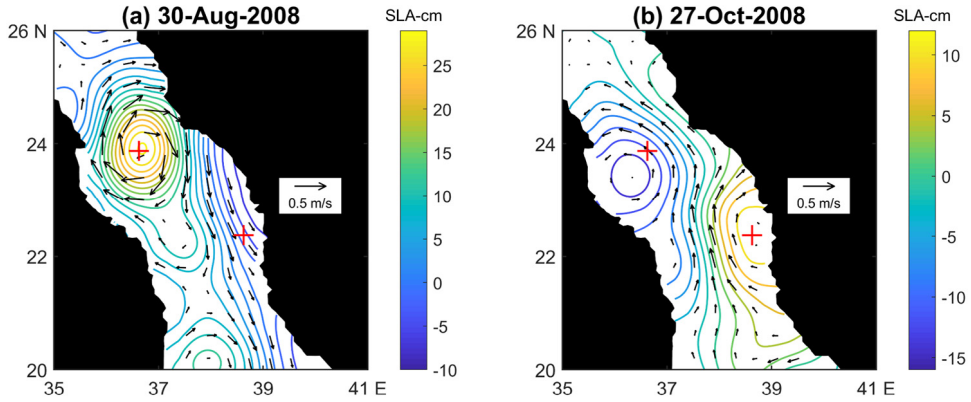

Fig. 9. Fields of sea level anomaly (SLA) on dates of maximum SLA difference between the two points indicated by red crosses (see Fig. 8). The vectors show the surface geostrophic velocity computed from the SLA fields.

modes show smaller-scale spatial variability (Fig. 4). It is likely that a sizable portion of the sea level variability not accounted for by the first EOF mode may be due to the formation and movement of basin-scale eddies and coastal boundary currents, which are prevalent in the Red Sea and occur over scales of order 100 km (Quadfasel and Baudner, 1993; Sofianos and Johns, 2007; Zhai and Bower, 2013; Chen and others, 2014; Zhan et al., 2014; Zarokanellos et al., 2017).

To demonstrate the impact of eddies and boundary currents on smaller-scale weather-band sea level variability, we consider how these features impact the difference in sea level at a point near Thuwal and at a point in the central Red Sea where the LFWB SLA has a relatively low correlation with the Thuwal pressure record (Fig. 4). The difference between the LFWB signals at these two sites is small, with an RMS value of 7 cm over the 2008–2011 period. However, the difference between the LFWB signal between these sites exceeds 25 cm on two occasions: 30 August and 27 October 2008 (Fig. 8). On 30 August, the difference in the SLA at the two sites is principally due to the SLA gradients associated with an anticyclonic eddy centered at roughly 36.67°E; 23.9°N and a coastal boundary current flowing southward offshore of Thuwal (Fig. 9a). In the SLA fields, the eddy forms and intensifies in the last week of August 2008 and dissipates in the first week of September. The SLA difference between the two sites on 27 October is principally due to the elevation gradient associated with a northward current flowing over the central Red Sea (Fig. 9b). In the SLA fields, the current forms in the week prior to 27 October and dissipates in the following week.

4. Discussion

A key finding of this study is that the weather-band variations of Red Sea water level are dominated by a single mode in which the water level rises and falls coherently over the full Red Sea. The flow through the Strait of Bab al Mandab needed balance the change in Red Sea water volume associated with this mode is not insignificant. The spatially averaged velocity through the narrowest channel of the strait (∼17 km wide and 150 m deep) required to balance the change in sea level associated with this dominant mode has an RMS value of ∼2 cm s^{-1} and maximum amplitude of ∼5 cm s^{-1}.

Although a one-dimensional barotropic model forced by the along-axis wind stress does not account for the full suite of dynamics influencing the weather-band sea level motions, it closely reproduces the weather-band fluctuations of the central Red Sea. The model predictions lead the observed sea level variations by roughly two days, making it a viable, and easily implemented, tool for short-term prediction of sea level. However, a more sophisticated model is needed to assess how variations in Red Sea water level are influenced by factors such as the earth's rotation, water column stratification and bathymetry.

In addition, a number of aspects of the weather-band sea level variations in the Red Sea system were not considered in our study. These include the coupling of sea level signal of the Red Sea with the adjoining Gulfs of Suez and Aqaba and the influence of mountain gap wind jets (Jiang et al., 2009; Zhai and Bower, 2013; Davis et al., 2015; Bower and Farrar, 2015) on local sea level variations.

Acknowledgments

For their support in maintaining the array of pressure sensors, the data from which were critical for our study, the authors thank personnel of the Coastal and Marine Resources Core Lab of King Abdullah University of Sciences and Technology (KAUST), especially Haitham Jahdali and Ramzi Jahdaali, as well as Yasser Kattan (KAUST) and Sean Whelan of the Woods Hole Oceanographic Institution (WHOI). The pressure sensor and meteorological buoy data were acquired as part of a program supported by Award Nos. USA00001, USA00002 and KSA00011 made by KAUST to WHOI. The data analysis and modeling work of this study were supported General Commission for Survey (GCS), under a project number RGC/3/1612-01-01 made by Office of Sponsored research (ORS)/KAUST, Kingdom of Saudi Arabia.

References

Abdelrahman, S.M., 1997. Seasonal fluctuations of mean sea level at Gizan, Red Sea. J. Coastal Res. 13, 1166–1172.

Bower, A.S., Farrar, J.T., 2015. Air–sea interaction and horizontal circulation in the Red Sea. In: Rasul, N.M.A., Stewart, I.C.F. (Eds.), The Red Sea, Springer Earth System Sciences. Springer-Verlag Berlin Heidelberg, http://dx.doi.org/10.1007/978-3-662-45201-1_1, 329-342.

Bruckner, A., Rowlands, G., Riegl, B., Purkis, S., Williams, A., Renaud, P., 2012. Khaled bin Sultan Living Oceans Foundation Atlas of Saudi Arabian Red Sea Marine Habitats. Panoramic Press, p. 262.

(12 others), Chen, C., et al., 2014. Process modeling studies of physical mechanisms of the formation of an anticyclonic eddy in the central Red Sea. J. Geophys. Res. Oceans 119, 1445–1464. http://dx.doi.org/10.1002/2013JC009351.

Csanady, G.T., 1973. Wind-induced barotropic motions in long lakes. J. Phys. Oceanogr. 3, 429–438.

Davis, K.A., Lentz, S.J., Pineda, J., Farrar, J.T., Starczak, V.R., Churchill, J.H., 2011. Observations of the thermal environment on Red Sea platform reefs: A heat budget analysis. Coral Reefs 30, 25–26. http://dx.doi.org/10.1007/s00338-011-0740-8.

Davis, S.R., Pratt, L.J., Jiang, H., 2015. The Tokar Gap jet: regional circulation, diurnal variability, and moisture transport based on numerical simulations. J. Clim. 28, 5885–5907.

Defant, A., 1961. Physical Oceanography, Volume 2. Pergamon Press, Oxford, p. 598.

DeVantier, L., Tourak, E., Al-Shaikh, K., De'ath, G., 2000. Coral communities of the central-northern Saudi Arabian Red Sea. Fauna of Arabia 18, 23–66.

Farrar, S., Lentz, J.T., Churchill, J., Bouchard, P., Smith, J., Kemp, J., Lord, J., Allsup, G., Hosom, D., 2009. King Abdullah University of Science and Technology (KAUST) mooring deployment cruise and fieldwork report. In: Technical Report. Woods Hole Oceanographic Institute, Woods Hole, Mass, p. 88.

Jarosz, E., Murray, S.P., Inoue, M., 2005. Observations on the characteristics of tides in the Bab el Mandab Strait. J. Geophys. Res. 110, C03015. http://dx.doi.org/10.1029/2004JC002299.

Jiang, H., Farrar, J.T., Beardsley, R.C., Chen, R., Chen, C., 2009. Zonal surface wind jets across the Red Sea due to mountain gap forcing along both sides of the Red Sea. Geophys. Res. Lett. 36, L19605.

Large, W., Pond, S., 1981. Open Ocean momentum flux measurements in moderate to strong winds. J. Phys. Oceanogr. 11, 324–336.

Lentz, S.J., Churchill, J.H., Davis, K.A., Farrar, J.T., Pineda, J., Starczak, V., 2016. The characteristics and dynamics of wave-driven flow across a platform coral reef in the Red Sea. J. Geophys. Res. 121, 1360–1376. http://dx.doi.org/10.1002/2015JC011141.

Lentz, S.J., Davis, K.A., Churchill, J.H., DeCarlo, T.M., 2017. Coral reef drag coefficients – water depth dependence. J. Phys. Oceanogr. 47, 1061–1075. http://dx.doi.org/10.1175/JPO-D-16-0248.1.

Limeburner, R., 1985. CODE-2: Moored array and large-scale data report. WHOI Technical Report 85–35, 234 pp.

Madah, F., Mayerle, R., Bruss, G., Bento, J., 2015. Characteristics of Tides in the Red Sea Region, a Numerical Model Study. Open J. Mar. Sci. 5, 193–209.

Manasrah, R., Hasanean, H.M., Al-Rousan, S., 2009. Spatial and seasonal variations of sea level in the Red Sea, 1958-2001. Ocean Sci. J. 44, 145–159.

McDonald, C.B., Koseff, J.R., Monismith, S.G., 2006. Effects of the depth to coral height ratio on drag coefficients for unidirectional flow over coral. Limn. Oceanogr. 51, 1294–1301.

Monismith, S.G., Herdman, L.M.M., Ahmerkamp, S., Hench, J.L., 2013. Wave transformation and wave-driven flow across a steep coral reef. J. Phys. Oceanogr. 43, 1356–1379.

Morcos, S.A., 1970. Physical and chemical oceanography of the Red Sea. Oceanography and Marine Biology Annual Review 8, 73–202.

Patzert, W.C., 1974. Wind-induced reversal in Red Sea circulation. Deep-Sea Res. 21, 109–121.

Pugh, D.T., Abualnaja, Y., 2015. Sea level changes. In: Rasul, N., Stuart, I. (Eds.), The Red Sea. The Formation, Morphology, and Environment of a Young Ocean Basin. Springer Publishing, Germany, http://dx.doi.org/10.1007/978-3-662-45201-1_18.

Quadfasel, D., Baudner, H., 1993. Gyre-scale circulation cells in the Red Sea. Oceanol. Acta 16, 221–229.

Sofianos, S., Johns, W., 2001. Wind induced sea level variability in the Red Sea. Geophys. Res. Lett. 28, 3175–3178.

Sofianos, S.S., Johns, W.E., 2007. Observations of the summer Red Sea circulation. J. Geophys. Res. 112, C06025. http://dx.doi.org/10.1029/2006JC003886.

Sultan, S.A.R., Ahmad, F., El-Hassan, A., 1995. Seasonal variations of the sea level in the central part of the Red Sea. Estuar. Coast Shelf Sci. 40, 1–8.

Sultan, S.A.R., Ahmad, F., Nassar, D., 1996. Relative contribution of external sources of mean sea-level variations at Port Sudan, Red Sea. Estuar. Coast Shelf Sci. 42, 19–30.

Vercelli, F., 1925. Richerche di oceanografia fisica eseguite della R.N. AMMIRAGILIO MAGNAGHI (1923–24), part I, Correnti e maree. Ann. Idrog. 11, 1–188.

Zarokanellos, N.D., Kurten, B., Churchill, J.H., Roder, C., Voolstra, C.R., Abualnaja, Y., Jones, B.H., 2017. Physical mechanisms routing nutrients in the central Red Sea. J. Geophy. Res. 12, 2. http://dx.doi.org/10.1002/2017JC013017.

Zhai, P., Bower, A.S., 2013. The response of the Red Sea to a strong wind jet near the Tokar Gap in summer. J. Geophys. Res. 118, 422–434. http://dx.doi.org/10.1029/2012JC008444.

Zhan, P., Subramanian, A.C., Yao, F., Hoteit, I., 2014. Eddies in the Red Sea: A statistical and dynamical study. J. Geophys. Res. 119, 3909–3925. http://dx.doi.org/10.1002/2013JC009563.